

Penetration of confined ceramics targets

S. Das^a, W. Ronan^{a,b}, H.N.G. Wadley^c, V.S. Deshpande^{a,*}

^a Department of Engineering, University of Cambridge, Trumpington Street, Cambridge CB2 1PZ, UK

^b Biomedical Engineering, National University of Ireland, Galway, Ireland

^c Department of Material Science & Engineering, School of Engineering and Applied Science, University of Virginia, Charlottesville, VA 22904, USA

ARTICLE INFO

Article history:

Received 28 August 2017

Received in revised form 31 October 2017

Accepted 1 November 2017

Available online 7 November 2017

ABSTRACT

We have investigated the penetration response of confined ceramic targets impacted by Tungsten long-rod projectiles in the so-called Lundberg test setup with the ceramic modelled using a mechanism-based constitutive model. The calculations accurately predict the three observed penetration regimes, viz. interface defeat, dwell followed by penetration and penetration with no/short dwell. More importantly, the calculations suggest that these regimes occur in both a ceramic target and a reference target where microcracking of the ceramic is artificially switched off. This is because penetration occurs by a spherical cavity expansion mechanism with the onset of continued penetration set by the attainment of either a critical size of a plastic or damage zone. The dwell time then correlates with the time required to establish this inelastic zone. The main influence of damage is to reduce the pressure required to setup this critical inelastic zone and thereby reduce the interface defeat velocity as well as increase the penetration rate for a given velocity above the interface defeat velocity. We further show that an increase in the downward force due to the backflow of the deforming impactor is not essential for a dwell regime to exist. The mechanism-based ceramic model includes three material length scales and we demonstrate that the penetration size effect reported in experiments is primarily associated with the length scale associated with rate dependent lattice plasticity and the critical size of the comminuted zone that is required to trigger granular flow. The material model is also used to probe the dependence of material properties such as strength and toughness on the penetration resistance. Two regimes of penetration, viz. a plasticity-dominated and a microcracking-dominated regime emerge from the calculations. These predictions suggest that increasing the strength rather than toughness of the Corbit-98 Alumina will have a greater beneficial influence on its penetration performance.

© 2017 Elsevier Ltd. All rights reserved.

1. Introduction

The application of ceramic-based armour ranges from protection of aircraft and personnel against small-calibre threats, to vehicle armour designed to defeat long-rod penetrators and shaped charges. A common experiment used in a laboratory setting to investigate the dynamic deformation/failure behaviour of ceramics involves impacting a specimen comprising a well-confined ceramic cylinder with a heavy metal long-rod penetrator as shown in Fig. 1a. Such setups, known in the literature as “Lundberg tests” [1], are extensively used to study the dynamic penetration properties of ceramics over relatively long time frames. In such tests, the confinement prevents/reduces the macroscopic cracking of the ceramic target, and the statistical effects of cracking are minimised. Moreover, in these high velocity experiments, the loading due to the long-rod is primarily hydrodynamic [2] and thus relatively easy to characterise.

Time-resolved penetration behaviour of ceramic armour has been extensively studied over the past 45 years using flash radiography [3–6]. In the Lundberg test, the penetration response is divided into three regimes based on the impact velocity v_0 (of either the long-rod or the target in a reverse ballistic test) as sketched in Fig. 1b. Below a critical impact velocity v_c , the long-rod erodes by radial flow on the target surface with no significant penetration. This phenomenon is referred to as *interface defeat*. For velocities slightly higher than v_c , a phase of projectile defeat (*dwell*) followed by penetration can be observed. The phase without penetration has been termed *dwell* since the penetrator “dwells” on the target surface for a duration called *dwell time*. As the impact velocity increases well beyond v_c , the dwell time decreases and eventually becomes too short to be measured [7].

The most-widely employed explanation for the existence of dwell is cracking-induced loss of penetration resistance of the target material. This explanation is mainly based on post-mortem examination of recovered targets [8,9]. A region of intense microcracking (comminution) and cone cracks immediately under the

* Corresponding author.

E-mail address: vds@eng.cam.ac.uk (V.S. Deshpande).

impact site was observed in cross sections of ceramic targets subjected to impacts just below the transition velocity. Consequently, it is widely thought that dwell persists for the time needed for the ceramic to transition from an intact to a damaged state [7,10,11]. However, some ambiguities remain in this explanation which include that while micro-cracking has been observed in Silicon Carbide (SiC), no comminution occurred in Tungsten Carbide (WC), and Boron Carbide (B₄C) targets even though they also display the phenomenon of dwell [4,9].

Cracking or more specifically cone cracking has been proposed to rationalise recent findings of a test structure size dependence of the penetration response. Lundberg et al. [12] performed penetration measurements on geometrically self-similar test setups where both the target and projectile were geometrically scaled. Their measurements of the interface defeat velocity of back supported, but otherwise unconfined SiC targets are plotted in Fig. 1c where the size of the setup is parameterised by the radius a of the long-rod. Size effects in the millimetre length scale were clearly observed, and Lundberg et al. [12] attributed this phenomenon to cone cracking of the ceramic target. In this hypothesis, the interface defeat velocity is set by the onset of cone cracking in the ceramic, which occurs at reduced pressure as the size increases. However, no computations of the penetration process have been reported to confirm this hypothesis.

Uth and Deshpande [13] performed scaled penetration experiments of the Lundberg test using vacuum grease for the target and water to provide the hydrodynamic loading. These experiments enabled the use of high speed video imaging to observe the key phenomena and demonstrated that the backflow of the impacting fluid due to deformation of the target resulted in an increase in the downward force, i.e. a strong fluid–structure interaction (FSI) effect. They then attributed the dwell time to the period required for the backflow to be established. However, the importance of such a FSI effect during ceramic target impact remains unclear.

The Lundberg test has been extensively analysed using phenomenological models of ceramics such as the Johnson and Holmquist (JH) [10] model. This model embodies a Drucker–Prager yield surface [14] that evolves with damage through the effective plastic strain (analogous to that in the Johnson–Cook model [15] for metals). The representation has multiple coefficients and exponents that require calibration through dynamic measurements and does not incorporate any microstructural characteristic (such as grain size) or other material properties such as toughness and hardness that influence penetration. Nevertheless, the model when used to simulate the Lundberg test does predict key phenomena including dwell followed by penetration. The model [10,16] indicates that dwell ends when a critical level of target damage is attained and thus while appropriate for SiC may not be adequate for ceramics such as WC and B₄C where dwell with no cracking is observed [4,9]. Moreover, the Johnson and Holmquist [10] model is unable to link the penetration performance of ceramics with fundamental material properties such as hardness and toughness.

Deshpande and Evans [17] developed a mechanism-based model for the deformation and fracture response of ceramics. This was later extended by Deshpande et al. [18] to include granular flow. Gamble et al. [19] and Compton et al. [20] calibrated this model for a Corbit-98 grade Alumina and demonstrated its fidelity in predicting both the quasi-static and dynamic indentation response. Subsequently, Holland et al. [21] have used this model for investigating the perforation response of steel–alumina bilayers. Here we employ the extended Deshpande et al. [18] model to investigate the penetration of confined ceramic targets. The aim here is not to model the precise details of the experiments, of which there are many variants, but rather a generic situation in order to investigate the fundamentals of the mechanisms operative during the penetration of the ceramics. In particular, the study

attempts to clarify the roles of (i) cracking and its relation to dwell; (ii) the observed specimen size effect and (iii) the influence of fundamental material properties such as hardness and toughness on the penetration resistance.

2. Model description

We analyse the so-called Lundberg problem of the penetration of a confined ceramic target by a Tungsten long-rod penetrator. There exist a range of variants of these tests including: (i) different ceramic materials including SiC, Alumina, WC etc.; (ii) tests with and without an outer steel confining casing; and (iii) tests carried out in either a reverse ballistic set-up where the target is fired onto the stationary long-rod or a forward ballistic situation where the initially stationary target is impacted normally and centrally at a velocity v_0 by a long rod of radius a , as sketched in Fig. 1a. The qualitative features of the short-time penetration responses are similar in all these tests and here the aim is to develop a physical understanding of the phenomena rather than analyse a particular test in detail. Thus, here we analyse a “generic” Lundberg test comprising a steel encased Alumina target impacted by a Tungsten long rod in a forward ballistic setting. While the reference material that is analysed is Alumina, the study also presents a parametric dependence of penetration response on material properties.

The axisymmetric problem analysed is sketched in Fig. 2a. It comprises a cylindrical ceramic target of height H and radius L encased in a high strength steel casing. This casing comprises three parts as shown in Fig. 2a: (i) a cylindrical jacket of inner radius L and thickness h_s and (ii) top and bottom caps of thickness $2h_t$. These three parts are press-fitted together around the ceramic cylinder. The long rod first penetrates the outer steel confinement and then impacts the surface of the ceramic. Penetration of the outer casing results in small reduction in the velocity of the long-rod and measurements are typically reported of the penetration into the ceramic as a function of time visualised by flash X-ray photographs [5]. Moreover, our aim here is to understand the process of penetration into the ceramics. Thus, we do not model penetration of the outer casing and report calculations where at time $t = 0$ the long-rod impacts the top surface of the ceramic at velocity v_0 (i.e. velocity v_0 should be interpreted as the velocity with which the projectile impact the ceramic surface having already eroded a hole in the outer casing). A central cylindrical hole of radius $2a$ [10] is thus included in the top cap to represent the cavity resulting from the initial penetration of casing by the long-rod. Renström et al. [2] have shown that after a short initial transient (when shock effects are present), loading due to the Tungsten long-rod is purely hydrodynamic with the long-rod exerting a pressure $p(r)$ on the target surface as sketched in the inset of Fig. 2b, where r is a radial distance measured from the central axis of the long-rod (Fig. 2a). This loading is assumed to be hydrodynamic such that in terms of the non-dimensional radial co-ordinate $\bar{r} \equiv r/a$

$$p(\bar{r}) = \frac{1}{2} \rho_p v_0^2 \bar{p}(\bar{r}), \quad (2.1)$$

where $\rho_p = 17.7 \times 10^3 \text{ kg m}^{-3}$ is the density of Tungsten and the non-dimensional pressure $\bar{p}(\bar{r})$ is sketched in Fig. 2b. The calculations of Renström et al. [2] show that $\bar{p}(0) \approx 1.2$ (where the factor of 1.2 is due to compressibility and finite strength of the Tungsten) with the pressure decreasing with increasing \bar{r} until $\bar{p}(2.5) \approx 0$. We performed finite element (FE) calculations of the penetration by applying this pressure distribution on the surface of the ceramic as opposed to explicitly modelling the long-rod/target interaction.

The penetration calculations were performed using the explicit version of the commercial FE package ABAQUS. The axisymmetric problem analysed is sketched in Fig. 2a and is unrestrained in the

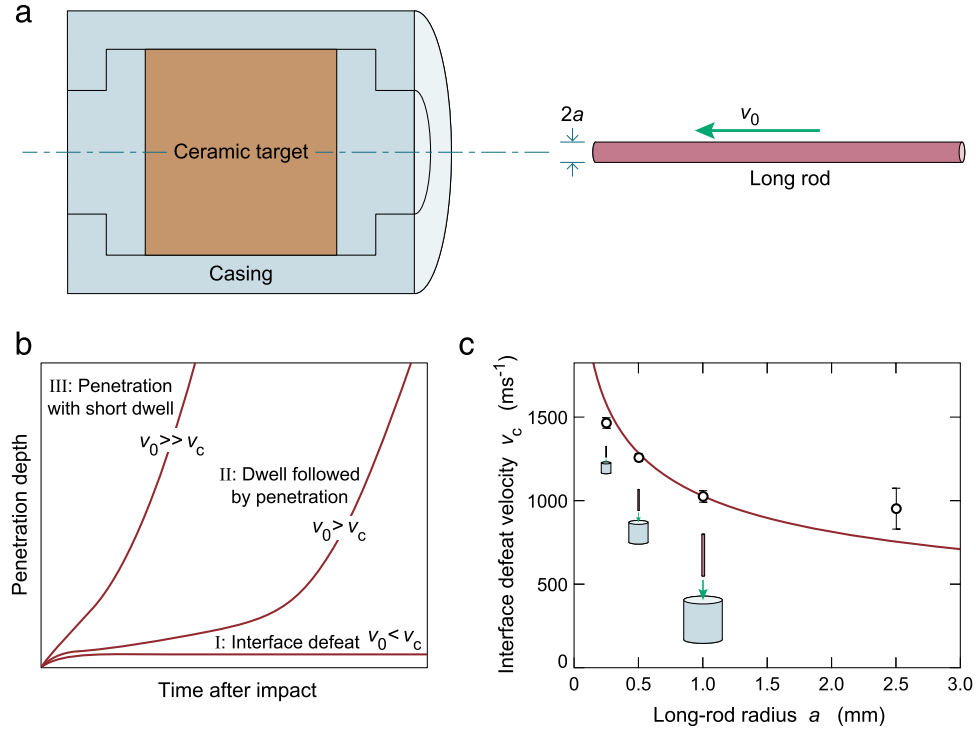


Fig. 1. (a) Sketch of the so-called Lundberg problem of the ballistic impact of a confined ceramic target by a Tungsten long-rod. (b) The three penetration regimes as a function of the impact velocity v_0 . (c) Target size dependence of the interface defeat velocity. Measurements from [12] are shown for geometrically self-similar targets and long-rods parameterised by the long-rod radius a . Note that while (a) and (b) are illustrative sketches, data from [12] is re-plotted in (c).

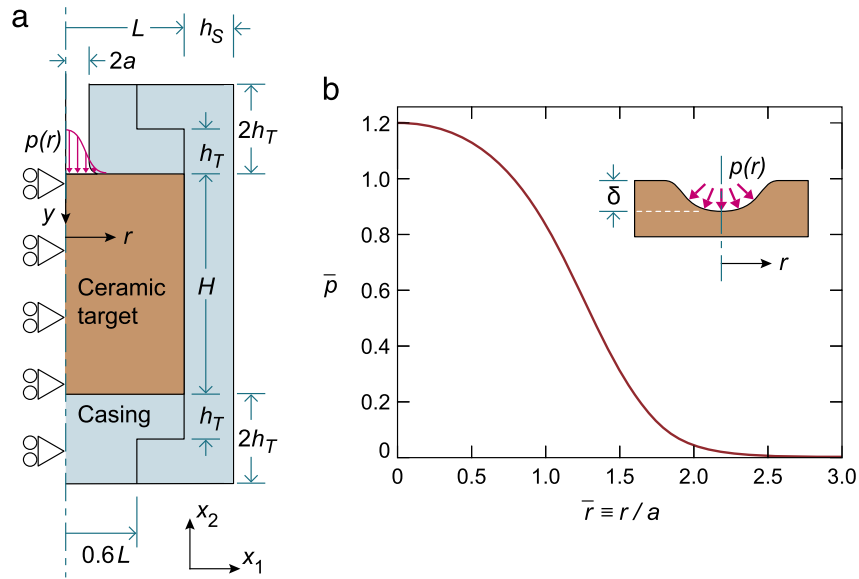


Fig. 2. (a) Sketch of the axisymmetric boundary value problem of the confined ceramic target with the imposed pressure load to simulate loading by the Tungsten long-rod. The definition of the co-ordinate y is included in the sketch. (b) Predictions of Renström et al. [2] for the non-dimensional pressure $\bar{p}(\bar{r})$ imposed by the long rod as a function of the non-dimensional radial co-ordinate $\bar{r} \equiv r/a$. The inset shows a sketch of the applied pressure on the deformed target surface and the definition of the penetration δ .

x_2 — direction consistent with the reverse ballistic Lundberg test. The target is discretised using a combination of 3-noded triangular and 4-noded quadrilateral elements with reduced integration. The mesh was graded such that both in the casing and target it was very fine near the imposed and coarsened away from the impact zone. The smallest element had leading dimensions $\sim L/200$. Mesh convergence studies confirmed that further mesh refinement did not change any of the reported penetration results by more than 2%. Hard contact was specified between all the press-fit surfaces in

the model, viz. between the ceramic and the casing and between the three parts that formed the casing (the geometry of the casing parts is included in Fig. 2a). The loading due to the Tungsten long-rod is imposed by specifying the pressure (2.1) on the deformed surface of the target as sketched in the inset of Fig. 2b via the VDLOAD user subroutine in ABAQUS. Since the loading applied is a pressure, the imposed resultant tractions were normal to the deformed surface with this pressure only dependent on the radial position r of the surface point in the deformed configuration. This

implies that the total downward force

$$F_D = 2\pi \int_0^\infty p(r)r \, dr, \quad (2.2)$$

imposed by the loading remains constant throughout the deformation history, i.e. any FSI effects due to backflow of the deforming Tungsten projectile are neglected. This is done so as to be able to investigate the effect of material and structural properties of the target without the complicating effects of FSI.

The casing of the target is typically made from a high strength steel and is approximated here as an isotropic elastic solid of density 7850 kgm^{-3} , Young's modulus 210 GPa and Poisson's ratio 0.3 . The ceramic on the other hand is modelled using a modified version of the mechanism-based ceramic model of Deshpande et al. [18].

2.1. Overview of the ceramic constitutive model

Here we give a brief description of the mechanism-based ceramic constitutive model of Deshpande et al. [18] with an emphasis on the modifications to the granular plasticity aspect of this model implemented in this investigation. This constitutive model was implemented in ABAQUS as a user material model via the VUMAT functionality. The inelastic deformation of polycrystalline ceramics occurs by three primary mechanisms proceeding partially in series and partially in parallel (Fig. 3). The ceramic is envisaged to contain a population of pre-existing flaws or heterogeneities that under stress can extend into microcracks. Before these microcracks form, plastic deformation can only occur by dislocation slip or twinning termed here as *lattice plasticity*. When microcracks grow and coalesce, the ceramic transitions into a granular medium comprising densely packed granules with dimensions typically dictated by the grain size. Thus, the total strain rate $\dot{\epsilon}_{ij}$ of the ceramic is written as the sum of the elastic strain rate $\dot{\epsilon}_{ij}^e$ and the deformation rates due to lattice plasticity $\dot{\epsilon}_{ij}^p$ as well as granular flow $\dot{\epsilon}_{ij}^g$, i.e.

$$\dot{\epsilon}_{ij} = \dot{\epsilon}_{ij}^e + \dot{\epsilon}_{ij}^p + \dot{\epsilon}_{ij}^g. \quad (2.3)$$

Elastic deformation is assumed to be governed by an isotropic Hooke's law with shear modulus G and Poisson's ratio ν that are not affected by the above three inelastic mechanisms. We proceed to briefly describe the constitutive relations for $\dot{\epsilon}_{ij}^p$ and $\dot{\epsilon}_{ij}^g$ with expression for some coefficients detailed in Appendix.

Lattice plasticity: Plastic flow (due to dislocation motion and twinning) is assumed to be described by a viscoplastic relation with the von-Mises effective stress σ_e governing the plastic strain rate and direction of plastic flow such that

$$\dot{\epsilon}_{ij}^p = \dot{\epsilon}_e^p \frac{\partial \sigma_e}{\partial \sigma_{ij}}, \quad (2.4)$$

where $\dot{\epsilon}_e^p$ is the effective plastic strain rate. Noting that at low strain rates plastic flow is governed by the Peierls resistance while at high strain rates phonon drag is the rate limiting process, Deshpande et al. [18] proposed a piecewise phenomenological relation for $\dot{\epsilon}_e^p$ given by

$$\frac{\dot{\epsilon}_e^p}{\dot{\epsilon}_0} = \begin{cases} \left(\frac{\dot{\epsilon}_0}{\dot{\epsilon}_t} \right)^{(1-n)/n} \left(\frac{2\sigma_e}{\sigma_0} - 1 \right) & 2\sigma_e > \sigma_0 \left[\left(\frac{\dot{\epsilon}_t}{\dot{\epsilon}_0} \right)^{1/n} + 1 \right] \\ \left(\frac{2\sigma_e}{\sigma_0} - 1 \right)^n & \sigma_0 < 2\sigma_e \leq \sigma_0 \left[\left(\frac{\dot{\epsilon}_t}{\dot{\epsilon}_0} \right)^{1/n} + 1 \right] \\ 0 & 2\sigma_e \leq \sigma_0, \end{cases} \quad (2.5)$$

where $\dot{\epsilon}_0$, $\dot{\epsilon}_t$ and n are a reference strain rate, the strain rate to transition to the phonon drag regime and a strain rate sensitivity

exponent respectively while $\sigma_0(\dot{\epsilon}_e^p)$ is the flow strength at equivalent plastic strain $\dot{\epsilon}_e^p$. The strain hardening function for this flow strength is expressed in terms of the uniaxial yield strength σ_Y and the strain hardening exponent M as

$$\sigma_0 = \frac{\sigma_Y}{2} \left[1 + \left(\frac{\dot{\epsilon}_e^p}{\dot{\epsilon}_0} \right)^M \right], \quad (2.6)$$

where $\dot{\epsilon}_0$ is a reference plastic strain at which $\sigma_0 = \sigma_Y$. We emphasise here that in the phonon drag regime with $\sigma_e \gg \sigma_0$, the plastic flow follows a linear viscous law such that $\sigma_e = \eta \dot{\epsilon}_e^p$, where the viscosity

$$\eta = \frac{\sigma_0}{2\dot{\epsilon}_0} \left(\frac{\dot{\epsilon}_t}{\dot{\epsilon}_0} \right)^{\frac{1-n}{n}}. \quad (2.7)$$

Under dynamic loading, this introduces a length scale ℓ_p into the problem that characterises the plastic shock width. Dimensional analysis dictates that this shock width is given by $\ell_p = \eta/(\rho \Delta v)$, where ρ is the density of the ceramic and Δv the velocity jump across the shock.

Microcrack evolution: The ceramic is assumed to contain an array of f microcracks per unit volume with each microcrack comprising two wing cracks of length l that develop from an initial flaw of radius c . The initial and current levels of damage are expressed as $D_0 \equiv (4/3)\pi(\alpha c)^3 f$ and $D \equiv (4/3)\pi(l + \alpha c)^3 f$, respectively where α is a flaw orientation factor. The evolution of the wing cracks (and thereby the damage) is governed by the mode-I stress intensity factor K_I at the microcracks. Deshpande and Evans [17] provided expressions for K_I in terms of coefficients A , B , C and E (see Appendix for the relevant formulae), the mean stress $\sigma_m \equiv \sigma_{kk}/3$ and the effective stress σ_e . In regime I, when the triaxiality $\lambda \equiv \sigma_m/\sigma_e \leq -B/A$, the cracks are shut with friction preventing sliding and thus $K_I = 0$. In regime II ($-B/A < \lambda < AB/(C^2 - A^2)$), friction cannot prevent crack face sliding such that

$$\frac{K_I}{\sqrt{\pi c}} = A\sigma_m + B\sigma_e. \quad (2.8)$$

In regime III where $\lambda \geq AB/(C^2 - A^2)$ the crack faces lose contact resulting in

$$\frac{K_I}{\sqrt{\pi c}} = \sqrt{C^2 \sigma_m^2 + E^2 \sigma_e^2}. \quad (2.9)$$

The wing cracks length grows at a rate \dot{l} related to these stress intensity factors via

$$\dot{l} = \begin{cases} \min \left[\dot{l}_0 \left(\frac{K_I}{K_{IC}} \right)^m, \sqrt{G/\rho} \right] & D < 1 \\ 0 & \text{otherwise,} \end{cases} \quad (2.10)$$

where K_{IC} is the mode I (short crack) fracture toughness of the ceramic while \dot{l}_0 is the crack growth rate at $K_I = K_{IC}$ and m the rate exponent for crack growth. In Eq. (2.10) the crack growth speed has been limited to the shear wave speed. Since $K_I \rightarrow \infty$ as the cracks fully coalesce (i.e. when $D \rightarrow 1$) we supplant the microcracking models with a granular plasticity model.

Granular plasticity: The comminuted ceramic is modelled as a granular medium using a non-associated Drucker–Prager type constitutive law, with an effective stress

$$\hat{\sigma} \equiv \frac{\sigma_e + (\tan \omega) \sigma_m}{1 - \frac{\tan \omega}{3}}, \quad (2.11)$$

where ω is the friction angle while the effective granular strain rate is related to the uniaxial compressive strength Σ_c of the ceramic via

$$\frac{\dot{\epsilon}_e^g}{\dot{\epsilon}_s} = \begin{cases} \left(\frac{\hat{\sigma}}{\Sigma_c} - 1 \right)^s & \hat{\sigma} > \Sigma_c \\ 0 & \text{otherwise,} \end{cases} \quad (2.12)$$

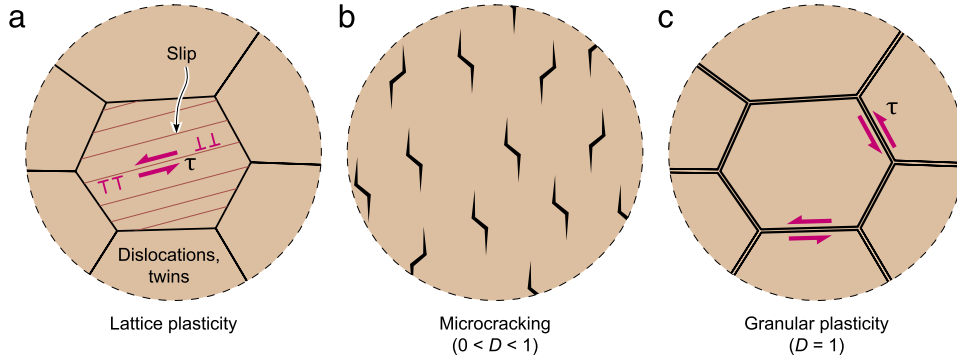


Fig. 3. Mechanisms of inelastic deformation and damage operative in polycrystalline ceramics under compressive stress states.

with $\dot{\epsilon}_s$ the reference strain rate and s a rate exponent. We take $s = 0.5$ for $\sigma_m \leq 0$ so that we recover the Bagnold [22] rate sensitivity of a granular medium and $s = 10$ for $\sigma_m > 0$ to ensure that granular plasticity has negligible rate sensitivity in the presence of tensile hydrostatic stresses. (The transition between these two regimes is implemented smoothly as specified in Deshpande et al. [18].) Granular flow is assumed to be incompressible such that the granular strain rate follows from a relation analogous to Eq. (2.4) with

$$\dot{\epsilon}_{ij}^g = \dot{\epsilon}_e^g \frac{\partial \sigma_e}{\partial \sigma_{ij}}. \quad (2.13)$$

For $\hat{\sigma} \gg \Sigma_c$ with $\sigma_m \leq 0$, Eq. (2.12) implies a quadratic rate dependence of the form

$$\hat{\sigma} = \frac{\Sigma_c}{\dot{\epsilon}_s^2} (\dot{\epsilon}_e^g)^2. \quad (2.14)$$

Dimensional analysis then specifies that under dynamic loading, there exists a length scale associated with granular plasticity given by

$$\ell_g = \frac{1}{\dot{\epsilon}_s} \sqrt{\frac{\Sigma_c}{\rho}}, \quad (2.15)$$

where ℓ_g can be interpreted as the width of shock front associated with granular plasticity.

2.1.1. Non-local damage and granular plasticity

In the approach proposed by Deshpande et al. [18] both lattice plasticity and granular plasticity are active for all stress states except that granular plasticity becomes dominant in the fully comminuted state. This is accomplished by decreasing Σ_c with increasing D , i.e. the damage parameter D calculated from the microcracking model serves to set the strength for granular flow. Deshpande et al. [18] used the local damage variable D but here we propose a non-local variant of their model based on the integral formulation as proposed by Bažant and Jirásek [23], Tvergaard and Needleman [24] and many others. There are two key reasons to make this modification:

- (i) Microcracking results in the formation of granules on the order of the grain size. However, for granular plasticity to occur in the continuum sense as described above, a multitude of cracked grains in a local area need to act in concert. Thus, granular flow will only occur if the damage $D = 1$ extends over a region of some finite size rather than just a local material point.
- (ii) Damage also results in a softening of the material and a loss of ellipticity of the governing equations. This usually results in predictions that are sensitive to the size and type of FE mesh. However, introducing a damage length scale by employing a non-local damage model alleviates the mesh dependency of the predictions.

Here we use an integral non-local formulation [23,24] wherein a non-local damage parameter $\bar{D}(x_i)$ is defined at location x_i via

$$\bar{D}(x_i) = \frac{1}{V_0} \int_{V_0} D dV, \quad (2.16)$$

where V_0 is a sphere of radius ℓ_D centred at x_i , i.e. the non-local damage variable $\bar{D}(x_i)$ is the volume average of D in the vicinity of x_i .¹ The integral (2.16) was evaluated by a Gaussian quadrature over all elements that were within the radius ℓ_D around x_i . To ensure numerical convergence it is therefore imperative that the FE element size e is much less than ℓ_D : in all calculations reported here $e < \ell_D/10$ in the region of the target where damage occurred.

In addition to the above numerical constraint, there is a physical constraint on ℓ_D , viz. the radius ℓ_D needs to be chosen to be much greater than the grain size of the polycrystalline ceramic to ensure that $\bar{D} = 1$ only when a sufficient number of grains in the vicinity of x_i have cracked for granular flow to be operative. With this constraint satisfied, we can then use \bar{D} to transition the ceramic from its undamaged state D_0 to the fully comminuted state wherein granular plasticity is the dominant deformation mode. This is performed using the following three relations.

The uniaxial strength is reduced from the plastic yield strength σ_0 to the fully comminuted strength σ_c via

$$\Sigma_c = \sigma_0 - (\sigma_0 - \sigma_c) \left(\frac{\bar{D} - D_0}{1 - D_0} \right)^q, \quad (2.17)$$

where q is an exponent that governs the rate of the transition. For consistency, the friction angle is also increased from $\omega = 0$ when $\bar{D} = D_0$ to its value ω_0 in the fully comminuted state using

$$\tan \omega = \frac{(\sigma_0 - \Sigma_c) \tan \omega_0}{\sigma_0 - \sigma_c \left(1 - \frac{\tan \omega_0}{3} \right) - \Sigma_c \frac{\tan \omega_0}{3}}. \quad (2.18)$$

Finally, the reference granular strain rate is increased from $\dot{\epsilon}_s = 0$ at $\bar{D} = D_0$ (i.e. no granular plasticity without microcracking) so that

$$\dot{\epsilon}_s = \dot{\epsilon}_{s0} \left(\frac{\bar{D} - D_0}{1 - D_0} \right)^q. \quad (2.19)$$

2.1.2. Target geometry and material parameters

The objective of the study is to develop a physical understanding of the penetration of confined ceramic targets as opposed to a direct comparison between numerical predictions and measurements. Thus, the simulations were designed to analyse

¹ At the edge of the domain the complete integral (2.16) cannot be unambiguously evaluated as part of the sphere may lie outside the ceramic. In such cases the volume V_0 is interpreted as that part of the sphere that lies inside the ceramic.

Table 1
Reference material parameters for the Alumina.

Parameter	Value
Shear modulus G	148 GPa
Poisson's ratio ν	0.239
Density ρ	3864 kg m ⁻³
Yield strength σ_Y	5.75 GPa
Fracture toughness, K_{IC}	3 MPa \sqrt{m}
Transition strain rate $\dot{\epsilon}_t$	10 ⁶ s ⁻¹
Strain hardening exponent M	0.1
Crack growth rate sensitivity exponent m	30
Strain rate dependence exponent n	34
Reference crack growth rate \dot{l}_0	0.01 ms ⁻¹
Reference plastic strain rate $\dot{\epsilon}_0$	10 ⁻³ s ⁻¹
Reference plastic strain ϵ_0	0.002
Initial damage D_0	8.57 $\times 10^{-4}$
Number of cracks per unit volume f	1.71 $\times 10^{14}$ m ⁻³
Crack orientation factor α	1/ $\sqrt{2}$
Friction angle ω_0	70°
Uniaxial compressive strength of comminuted ceramic σ_c	1 MPa
Granular transition exponent q	5
Granular reference strain rate $\dot{\epsilon}_{s0}$	2 $\times 10^6$ s ⁻¹

a general problem in the class of problems posed by Lundberg and co-workers [1,5,6] rather than mimic one of their specific experiments. The intent is to vary both the target geometry and its material properties to investigate the dependence of the penetration response on these properties. Since Gamble et al. [19] and Compton et al. [20] have calibrated the Deshpande et al. [18] ceramic constitutive model against a range of experiments on the Corbit-98 Alumina, this motivates our choice for this ceramic to serve as a reference. Here we detail the reference target geometry and ceramic properties that are chosen to represent the Corbit-98 fine-grained Alumina (grain size $d \sim 3 \mu\text{m}$).

The reference properties of the Alumina are listed in Table 1. These parameters imply that the lattice plasticity length scale $\ell_p \approx 0.8 \text{ mm}$ assuming $\Delta v = v_0$ with a typical impact velocity $v_0 = 1730 \text{ ms}^{-1}$ and $\sigma_0 = \sigma_Y$. On the other hand, the granular plasticity length scale is much smaller with $\ell_g \approx 8 \mu\text{m}$ assuming $\Sigma_c = \sigma_c$. The damage length scale ℓ_D was not present in the model employed by Gamble et al. [19] and Compton et al. [20] (i.e. they implicitly set $\ell_D = 0$) and therefore needs to be independently selected for this study. Here we used a reference value of $\ell_D = 0.2 \text{ mm}$ so that $\ell_D/d \approx 70$, where $d = 3 \mu\text{m}$ is the grain size of the reference Alumina, i.e. we argue that granular flow can occur when all grains within a sphere of radius approximately $70d$ are cracked. Nevertheless, parametric studies of the sensitivity of the prediction to ℓ_D are also reported.

Unless otherwise specified, results are presented for two classes of materials: (i) the Alumina described by the material properties listed in Table 1 and (ii) a reference non-damaging ceramic with properties identical to Alumina except that microcracking is switched off by setting $K_{IC} = \infty$. This reference is used to isolate the effect of cracking on the penetration response.

3. Experimental validation of the model

The aim of this study is to investigate fundamentals of the deformation and failure mechanisms operative during the penetration of the ceramics in a long-rod penetration test rather than model a specific experiment. However, prior to proceeding with the generic study it is important to confirm the validity of the approach and importantly the material model in capturing experimental observations.

The material model described in Section 2 has been validated against a series of experiments of steel balls impacting Alumina targets [20]. However, this validation was conducted in a relatively low velocity regime (impact velocities typically less than

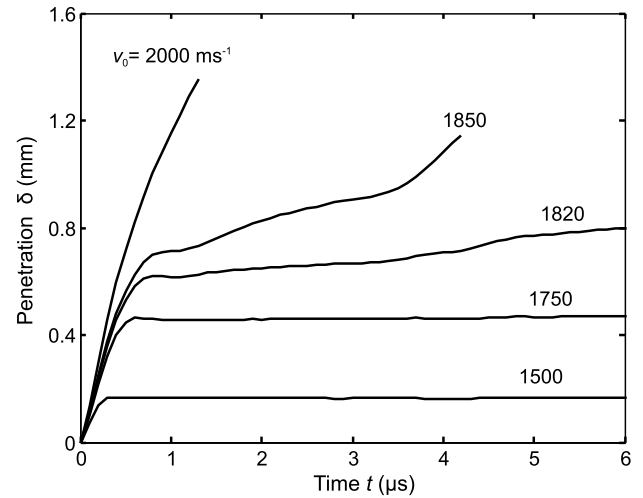


Fig. 4. Predictions of the temporal evolution of the penetration $\delta(t)$ into Alumina targets representative of the experiments of Subramanian and Bless [25].

400 ms⁻¹) and relatively shallow penetration depths. The long-rod experiments are typically in the 1500 ms⁻¹ range and accompanied by deep penetration. Here we have modified the model of Deshpande et al. [18] to include a non-local granular plasticity law to better capture the deformation processes during deep penetration. A validation of this new model against appropriate long-rod penetration data is presented in this section.

Subramanian and Bless [25] have reported measurements for confined Alumina targets of radius $L = 12 \text{ mm}$ and height $H = 38 \text{ mm}$ impacted by Tungsten long rods of radius $a = 0.4 \text{ mm}$. The Alumina cylinder on [25] was encased in a steel jacket of thickness $h_s = 2.5 \text{ mm}$ while the top and bottom caps had dimension $h_T = 1.6 \text{ mm}$. Subramanian and Bless [25] reported that an impact experiment with $v_0 = 1500 \text{ ms}^{-1}$ resulted in interface defeat while target penetration ensued at a Tungsten long-rod impact velocity $v_0 = 1750 \text{ ms}^{-1}$. We conducted penetration simulations using the setup shown in Fig. 2a and dimensions identical to the setup of Subramanian and Bless [25]. Loading due to the long-rod was imposed by applying a pressure $p(r)$ on the target as detailed in Section 2. Predictions of the penetration versus time response are included in Fig. 4 for v_0 in the range $1500 \text{ ms}^{-1} \leq v_0 \leq 2000 \text{ ms}^{-1}$. Here the penetration $\delta(t)$ is the depth at the centre of the surface of the target with respect to the undeformed surface of the target (inset of Fig. 2b) and time $t = 0$ corresponds to the instant the pressure was applied. After a small initial deformation, the penetration is arrested for $v_0 = 1500 \text{ ms}^{-1}$ in line with the observation of interface defeat at this velocity. Further, much in line with the observations reported in [25] continued penetration after a short dwell period is predicted for impact at $v_0 = 1850 \text{ ms}^{-1}$ (i.e. the predicted penetration velocity is about 5% higher than that reported in [25]). This agreement is obtained in spite of numerous simplifications in the model that include: (i) not explicitly modelling the Tungsten long-rod and the penetration through the steel top-cap and (ii) restricting the model to axi-symmetric states such that radial cracking is excluded. In fact radial cracking was also observed in the low velocity experiments reported in [20] but again an axisymmetric model sufficed to capture the majority of observations. We thus conclude that the relatively simple model developed here has sufficient fidelity to capture the critical deformation and failure mechanisms in the Lundberg test. We shall thus proceed to use this model to perform parametric studies to develop a fundamental understanding of the penetration process.

4. Parametric predictions of the penetration response

The main aims of the numerical study are:

- Develop an understanding of the dwell phenomenon and the associated dwell time.
- Understand the origins of the size effect of the penetration resistance.
- Relate fundamental material properties of a ceramic (such as its strength and toughness) to the penetration resistance in a Lundberg test.

With this in mind three sets of non-dimensional quantities are defined to aid the investigation:

(a) *Non-dimensional structural length-scales*: These are the specimen aspect ratio H/L , the non-dimensional casing thickness h/L and the ratio of the specimen to long-rod radii L/a .

(b) *Non-dimensional material length scales*: The ratio of structural loading length scale to material length scales will govern material size effects in the penetration response. With the radius of a long-rod being the primary loading length scale, we define ℓ_D/a , ℓ_p/a and ℓ_g/a as the non-dimensional material length scales associated with damage, lattice plasticity and granular plasticity respectively.

(c) *Non-dimensional material properties*: The key ceramic material parameters are the yield strength and toughness. The non-dimensional groups associated with strength and toughness are σ_Y/E and $K_{IC}/(E\sqrt{\pi d})$, respectively.

The three aims discussed above can be addressed by varying each of these groups in turn. Unless otherwise specified, all material parameters are held fixed at the values listed in Section 2.1.2 (i.e. alumina and the reference non-damaging ceramic) and calculations are presented for loading via a Tungsten long rod of radius $a = 1$ mm with ceramic cylinders of aspect ratio $H/L = 2$. The targets had a casing with thickness $h = h_S = h_T$ and $h/L = 0.4$. All results are presented in terms of the impact velocity v_0 of the long rod with calculations performed by applying a pressure $p(r)$ on the target as detailed in Section 2.

4.1. The origins of interface defeat and dwell

With the aim being to develop an understanding of interface defeat and dwell, we first consider the reference non-cracking ceramic in order to isolate the effect of microcracking and vary the structural length scale L/a . Since a is held fixed at 1 mm this implies we are changing the target size relative to the impacting long-rod while all other non-dimensional groups are held fixed. Predictions of penetration δ versus time t for the $L/a = 5$ and 10 targets comprising the reference non-damaging ceramic are plotted in Fig. 5a and b, respectively. The predictions clearly show the three regimes discussed in the introduction, viz. (i) an interface defeat regime where after some initial penetration no further penetration is observed for impact velocities below a critical value v_c ; (ii) at intermediate velocities there is a dwell regime followed by a sudden onset of penetration and (iii) a penetration regime at high velocities where penetration occurs with no intervening period of dwell. The key finding is that both the $L/a = 5$ and 10 targets have a similar response except that the long-rod impact velocities are all lower for the same penetration behaviour in the smaller target. For example, the interface defeat velocity v_c is lower in the $L/a = 5$ target compared to the larger $L/a = 10$ target and thus for a given impact velocity v_0 the dwell time is longer in the larger target. We proceed to investigate the physics behind these numerical observations.

The evolution of the deformation and equivalent plastic strain ϵ_p^p around the impact site in the $L/a = 10$ target are shown in Fig. 6a and b for impact velocities $v_0 = 1800$ ms⁻¹ and 1900 ms⁻¹,

respectively. An approximately spherical plastic zone is seen to propagate from the impact site. The evolution of this zone halts at $t \approx 2$ μ s for the $v_0 = 1800$ ms⁻¹ case consistent with interface defeat observed in Fig. 5b. However, the plastic zone continues to evolve in the $v_0 = 1900$ ms⁻¹ in line with the continued penetration predicted for this velocity (Fig. 5b). To further illustrate the evolution of the plastic zone we include in Fig. 7a and b plots of the variation of the effective plastic strain ϵ_p^p along the central axis of the target at selected times t for the $L/a = 5$ and 10 targets, respectively. In Fig. 7, the co-ordinate y is the distance below the target surface in the undeformed configuration along $r = 0$ (Fig. 2a). An impact velocity $v_0 = 1800$ ms⁻¹ is in the interface defeat regime for both the $L/a = 5$ and 10 targets and a comparison between Fig. 7a and b suggests that the final plastic zones are very similar. By contrast, $v_0 = 1900$ ms⁻¹ is in the penetration without dwell regime for the $L/a = 5$ target but in the dwell regime for the larger target. Nevertheless at the point where steady penetration commences in both targets (at $t \approx 2$ μ s for the smaller target and $t \approx 10$ μ s for the larger target), the plastic strain distributions within the targets are very similar. We now employ these observations to rationalise both the target size dependence of the response as well the fact that we get dwell followed by penetration for loading with a constant downward force, i.e. with no FSI effect as in Uth and Deshpande [13].

In the interface defeat regime, while the loading due to the long-rod is hydrodynamic, the ceramic target is deforming nearly quasi-statically with in fact deformation rates within the ceramic tending to zero at large times. Thus, the spherical expansion of the plastic zone in Fig. 6 is consistent with the Bishop et al. [26] quasi-static hypothesis that deep penetration of a plastic solid occurs by the expansion of a cavity from a radius of zero to the radius a of the penetrating punch. In a sphere with initial outer radius b_0 , the steady pressure p_{ss} required for this expansion given as by [27]

$$p_{ss} = 2\sigma_Y \ln\left(\frac{\xi}{a}\right) + \frac{2\sigma_Y}{3} \left[1 - \left(\frac{\xi}{b_0}\right)^3\right], \quad (4.1)$$

where ξ is the radius of plastic zone as sketched in Fig. 8. Moreover, for the expansion of a cavity of zero initial radius, the ratio ξ/a is independent of b_0 and given by

$$\frac{\xi}{a} = \left[\frac{E}{3(1-\nu)\sigma_Y}\right]^{1/3}, \quad (4.2)$$

i.e. as per the Bishop et al. [26] hypothesis continued penetration occurs when the plastic zone attains the critical value given by Eq. (4.2) independent of the target size. This is consistent with the numerical results in Fig. 7. Moreover, the minimum pressure p_c required to ensure continued penetration is given by substituting Eq. (4.2) into Eq. (4.1). Then interpreting b_0 with the radius L of the target we obtain

$$p_c = \frac{2\sigma_Y}{3} \left[1 + \ln\left(\frac{E}{3(1-\nu)\sigma_Y}\right) - \left(\frac{a}{L}\right)^3 \left(\frac{E}{3(1-\nu)\sigma_Y}\right)\right], \quad (4.3)$$

and an estimate for the interface defeat velocity then follows from Eq. (2.1) as

$$v_c \approx \sqrt{\frac{2p_c}{\rho_p}}. \quad (4.4)$$

Consistent with the numerical results in Fig. 5a and b, Eqs. (4.3) and (4.4) predict that v_c decreases with decreasing target size L/a . The three regimes of penetration can be rationalised as follows. Below v_c there is insufficient pressure to allow continued penetration by the expansion of the spherical cavity while for higher impact velocities, the pressure is sufficient to develop a plastic zone of size ξ given by Eq. (4.2). However, this zone takes a finite

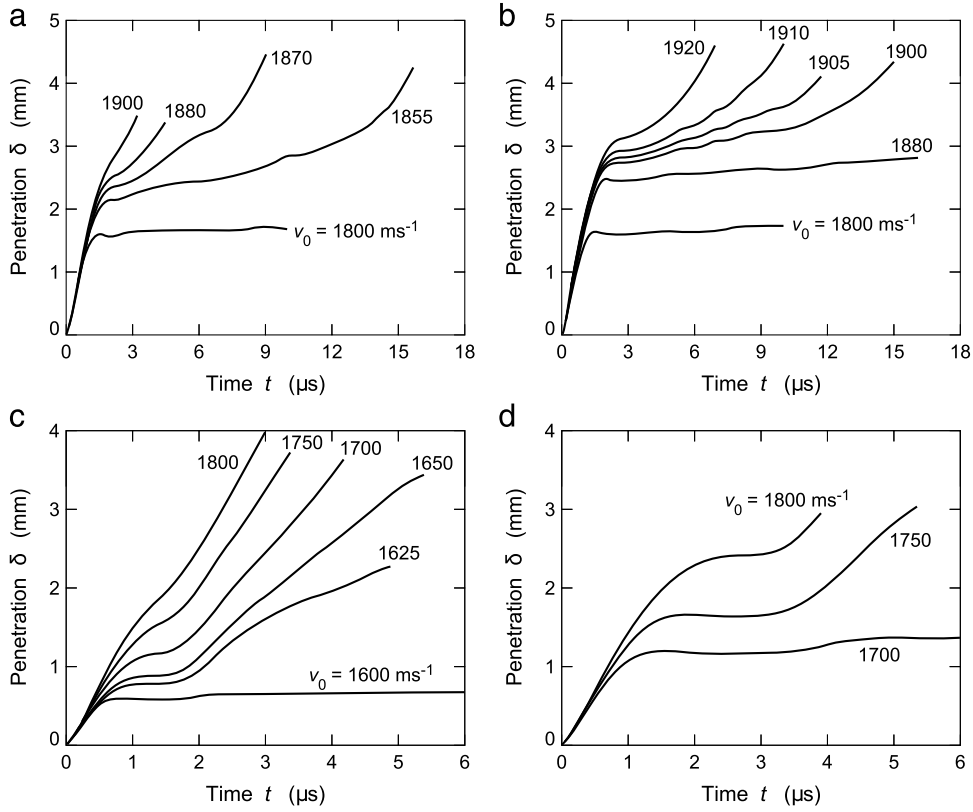


Fig. 5. Predictions of the temporal evolution of the penetration $\delta(t)$ into the reference non-damaging ceramic for the (a) $L/a = 5$ and (b) $L/a = 10$ targets with time $t = 0$ corresponding to the instant the pressure was first applied on the surface of the ceramic. The equivalent predictions for the (c) $L/a = 5$ and (d) $L/a = 10$ Alumina targets. In each case a selection of impact velocities v_0 are included ranging from interface defeat to penetration with no or short dwell times.

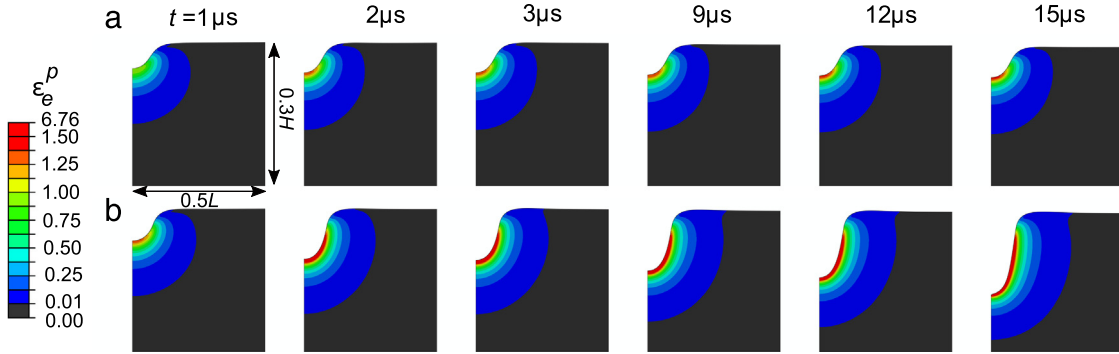


Fig. 6. Evolution of the equivalent plastic strain ε_e^p around the impact site in the $L/a = 10$ target comprising the reference non-damaging ceramic for impact velocities (a) $v_0 = 1800 \text{ ms}^{-1}$ and (b) $v_0 = 1900 \text{ ms}^{-1}$. The plastic strain distributions are shown at six selected times t with $t = 0$ corresponding to the instant the pressure was first applied on the surface of the ceramic.

time to establish and this is the dwell period of the response. The propagation of the plastic wave that sets this plastic zone is impact velocity dependent due to the rate sensitivity of the plastic response, and hence the dwell time decreases with increasing v_0 until penetration occurs without any noticeable dwell period. Since v_c decreases with decreasing L/a it follows that all these responses are shifted to lower velocities for the smaller targets. It is important to emphasise that while the spherical cavity expansion explanation based on Eqs. (4.1)–(4.4) is qualitatively accurate, quantitative agreement with the numerical results is not to be expected. This is because the real target is a rate sensitive and strain hardening plastic material surrounded by an elastic casing. The simple plastic cavity expansion expressions detailed above are for a rate independent, non-hardening solid and of course neglect the outer casing of a confined target. We have thus shown that

the regimes of the penetration response are at-least qualitatively reproduced in a target without cracking mechanisms. Moreover, the dwell behaviour is not necessarily caused by an FSI effect but rather related to the time required for the plastic zone to acquire a critical size. Of course, backflow of the deforming Tungsten long-rod and the consequent increase in the downward force resulting in a FSI effect will further increase penetration rates as discussed in Uth and Deshpande [13].

An immediate question that then arises is: what is the effect of cracking/damage that is commonly argued [10,16] to be critical in such experiments on ceramic targets? Numerical predictions of the penetration response of an Alumina target are included in Fig. 5c and d for the $L/a = 5$ and 10 targets. The qualitative responses are very similar to the case of the non-damaging targets with the three regimes of behaviour observed. However, all the impact

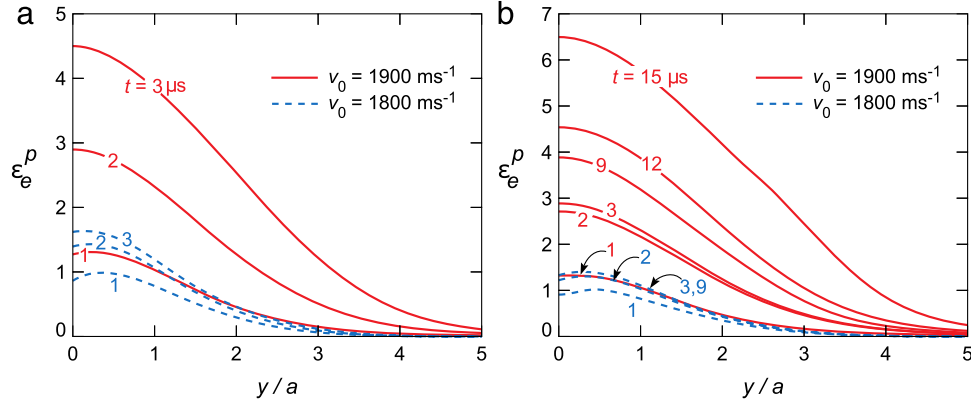


Fig. 7. Predictions of the plastic strain distributions along the normalised co-ordinate y/a , where y is measured along the central axis of the target below the impact site as sketched in Fig. 2a. Results are shown at selected times t for impact velocities $v_0 = 1800 \text{ ms}^{-1}$ and 1900 ms^{-1} in the (a) $L/a = 5$ and (b) $L/a = 10$ targets comprising the reference non-damaging ceramic. Time $t = 0$ corresponds to the instant the pressure was first applied on the surface of the ceramic.

velocities in Fig. 5c and d are lower than their corresponding values in Fig. 5a and b. The deformation of the $L/a = 10$ targets impacted at $v_0 = 1700 \text{ ms}^{-1}$ (interface defeat) and 1750 ms^{-1} (dwell followed by penetration) is included in Figs. 9 and 10 with contours showing the distribution of damage D and equivalent plastic strain ε_e^p , respectively. Now spherical expansions of both a damage zone and plastic zone are observed and it follows that the physical origins of the three regimes are similar to that discussed for non-damaging target materials. However, a crucial difference exists. The governing softening process in Alumina is now a combination of damage and lattice plasticity and hence penetration occurs when the overall inelastic zone containing damage and lattice plasticity attains a critical size with the dwell time governed by the time for this inelastic zone to establish. Thus, the interface defeat velocity and consequently all the other velocities in Fig. 5c and d are lower than the corresponding velocities in Fig. 5a and b as damage reduces the strength of the target and permits easier penetration. These numerical calculations are in agreement with previous hypotheses [10,16] that the dwell time in ceramic targets is set by the time for a damage zone to grow to a critical size. However, this damage is not essential, and the same phenomena can occur via only lattice plasticity. This is consistent with the no comminution observed in WC, and B_4C targets although of course we recognise that a direct analogy may not be appropriate as other deformation mechanisms such as phase transformations might be prevalent in ceramics such as B_4C .

4.2. The structural/material size effect

The structural size effect (Fig. 1c) wherein the interface defeat velocity increases with decreasing long-rod radius in geometrically self-similar specimens suggests that internal material length scale(s) dependent effects are operative. Such size effects are well-known in crystalline metals where the strength in compression, bending, torsion and indentation [28] has been found to increase with decreasing structural size. This size effect is related to length scales associated with dislocation structures in crystalline metals and is typically not operative for structural lengths greater than a few microns. The structural size effect in Fig. 1c is operative in the millimetre length scale and thus cannot be related to this well-established dislocation structure related size effects. Other rationalisations such as statistical variations of flaws [12] too are problematic since these flaws are present at spacings on the order of the grain size which again suggests that these size effects would be absent in the millimetre length scale. Nevertheless, no full scale penetration calculations have been reported to-date to probe the origins of this size effect and this is the focus here.

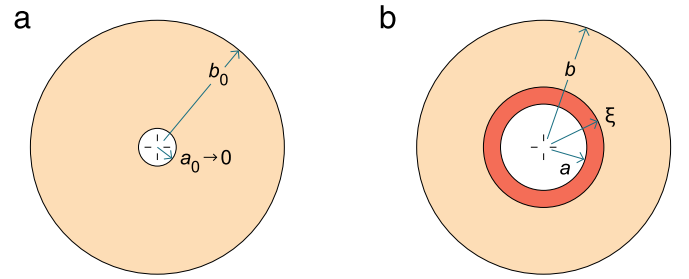


Fig. 8. The spherical cavity expansion analogy used by Bishop et al. [26] to analyse the deep penetration problem. (a) The undeformed sphere of outer radius b_0 and an incipient spherical cavity of radius $a_0 \rightarrow 0$. (b) The deformed sphere with a spherical cavity of radius a equal to the penetrator radius and a plastic zone of radius ξ .

There are three material length scales ℓ_p , ℓ_D and ℓ_g as discussed above. For the Alumina material parameters listed in Section 2.1.2, ℓ_p and ℓ_D are in the millimetre range and thus could be the source of the observed size effect. On the other hand, $\ell_g \approx 8 \mu\text{m}$ and thus for structural sizes in the millimetre range it is reasonable to assume $\ell_g = 0$. We thus investigate the effect of ℓ_p/a and ℓ_D/a on the penetration performance. In these calculations all material parameters except ℓ_D are held fixed.

(i) The effect of the damage length scale ℓ_D was investigated by varying ℓ_D keeping all other structural parameters fixed at their reference value. This permitted an investigation of the effect of ℓ_D/a with ℓ_p/a held fixed.

(ii) The effect of the plasticity length scale was investigated by varying the structural size while keeping L/a and H/L fixed at their reference values while changing a . This permitted an investigation of the effect of ℓ_p/a . For each value of ℓ_p/a , ℓ_D was varied to keep ℓ_D/a fixed.

The effect of material length scales on the penetration performance is illustrated in Fig. 11a showing the predicted variation of the non-dimensional penetration δ/a with non-dimensional time $\bar{t} \equiv c_e t/L$. Here $c_e \equiv \sqrt{2G(1+\nu)}/\rho$ is the longitudinal elastic wave speed in the Alumina. The results are all for a Tungsten long-rod impacting at $v_0 = 1730 \text{ ms}^{-1}$ and computed for selected choices of the material length scales ℓ_D/a and ℓ_p/a . The results are plotted in non-dimensional form such that all these penetration curves would collapse onto a single curve in the absence of any material size effect. However, it is clear the penetration decreases with increasing ℓ_p/a and ℓ_D/a , i.e. for a given ℓ_p and ℓ_D the penetration reduces with decreasing size a of geometrically self-similar targets. This “size effect” can be understood as follows.

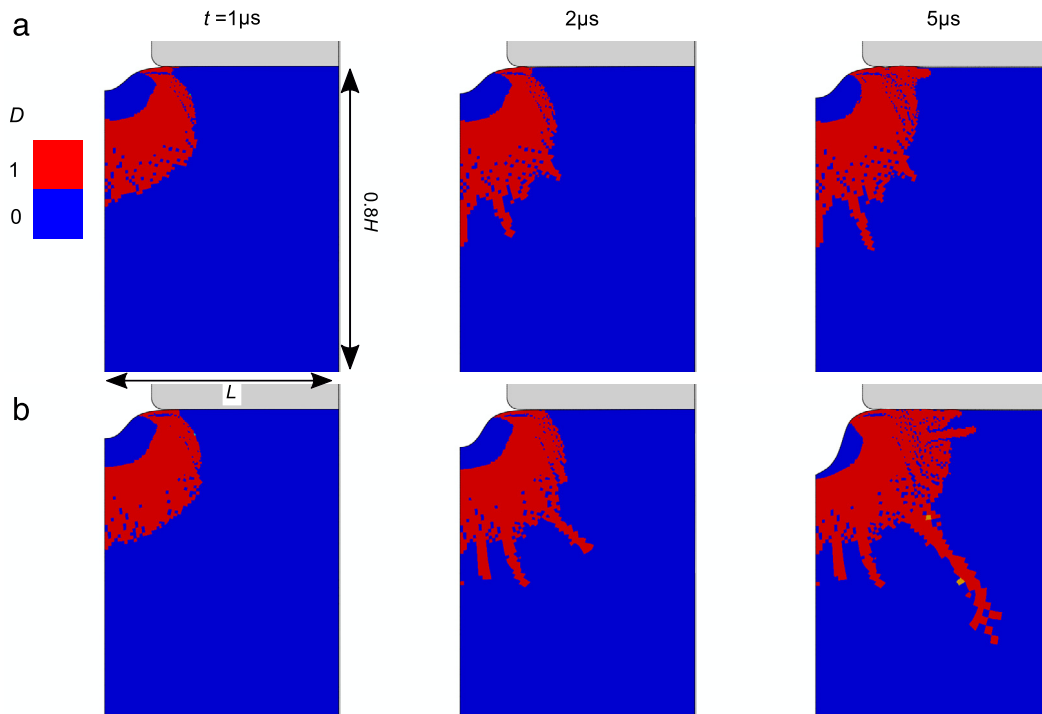


Fig. 9. Evolution of the damage D around the impact site in the $L/a = 10$ Alumina target for impact velocities (a) $v_0 = 1700 \text{ ms}^{-1}$ and (b) $v_0 = 1750 \text{ ms}^{-1}$. The damage distributions are shown at three selected times t with $t = 0$ corresponding to the instant the pressure was first applied on the surface of the ceramic.

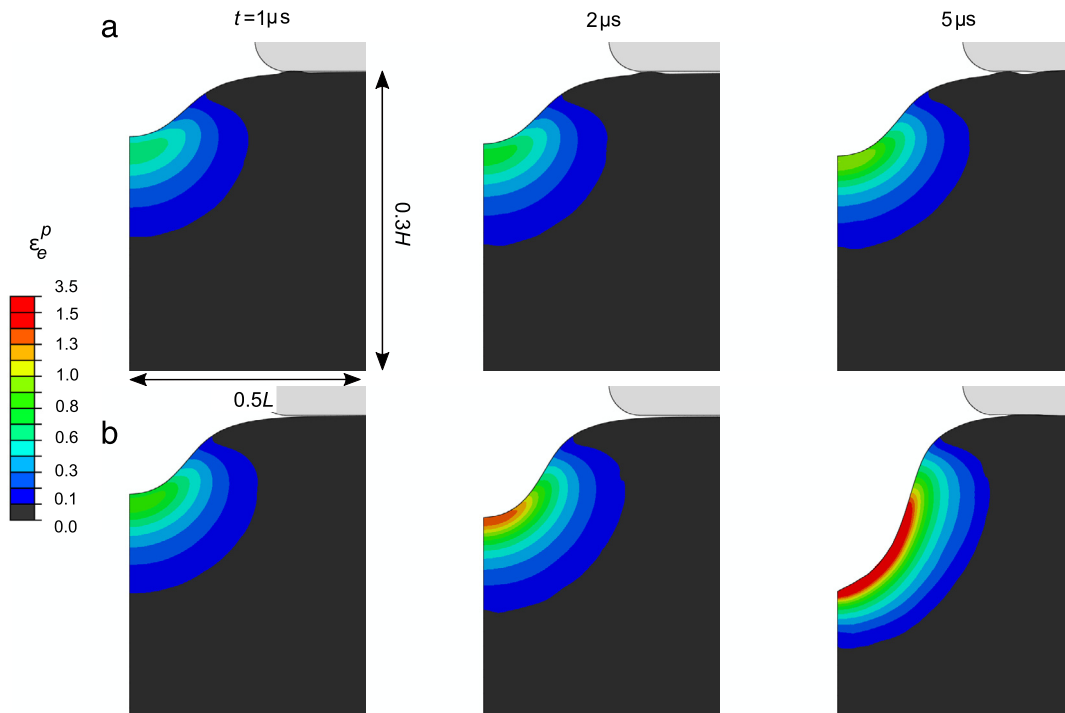


Fig. 10. Evolution of the equivalent plastic strain ϵ_e^p around the impact site in the $L/a = 10$ Alumina target for impact velocities (a) $v_0 = 1700 \text{ ms}^{-1}$ and (b) $v_0 = 1750 \text{ ms}^{-1}$. The plastic strain distributions are shown at three selected times t with $t = 0$ corresponding to the instant the pressure was first applied on the surface of the ceramic.

Increasing ℓ_p implies a larger effect of material viscosity which in turn increases material strength and thereby reduces penetration for a given impact velocity. Similarly, a larger ℓ_D means that a high stress is required over a larger volume of the material in order to cause softening of the material by cracking. This also has the net effect of strengthening the material.

The calculations predict a structural size effect with smaller, geometrically self-similar targets becoming increasingly harder to penetrate. In order to make more direct contact with the measurement shown in Fig. 1c, predictions of the interface defeat velocity v_c are included in Fig. 11b for geometrically self-similar Alumina targets parameterised by the radius a of the Tungsten long-rod.

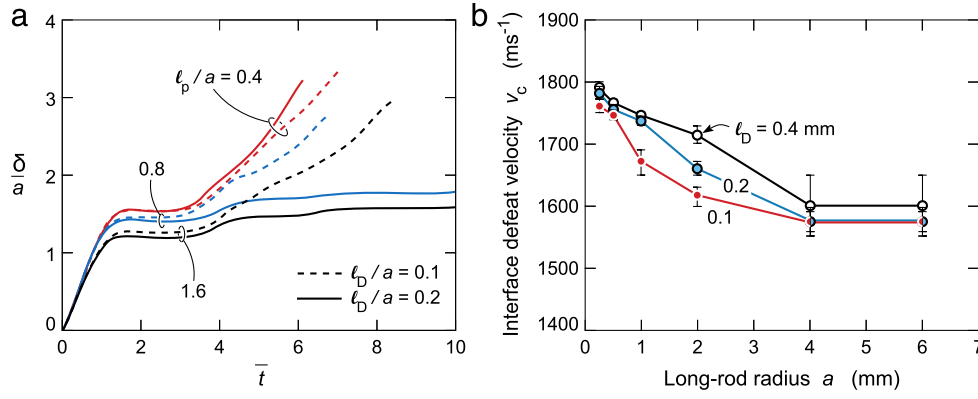


Fig. 11. (a) Predictions of the temporal evolution of the normalised penetration δ/a with normalised time \bar{t} for the Alumina target impacted at $v_0 = 1730 \text{ ms}^{-1}$. Results are shown for selected choices of the normalised plasticity length scale ℓ_p/a and damage length scale ℓ_D/a . The choice of the normalisation is such that in the absence of material size effects all these curves would collapse into a single master curve. (b) Predictions of the interface defeat velocity v_c for geometrically self-similar Alumina targets whose size is parameterised by the long-rod radius a . Results are shown for three choices of the damage length scale ℓ_D with the error bars denoting the range within which v_c was determined by the numerical calculations.

Results are shown in Fig. 11b for three choices of the damage length ℓ_D . Consistent with experimental measurements (Fig. 1c), v_c decreases with increasing a and plateaus out for $a \geq 4 \text{ mm}$ for all ℓ_D values considered here. Moreover, v_c increases with increasing ℓ_D for a given a . We emphasise that in Fig. 11b, for a given ℓ_D , the drop in v_c with increasing a is due to both the plasticity and damage length scales as both ℓ_p/a and ℓ_D/a decrease with increasing target size.

4.3. Effect of material properties on penetration response

The analysis of the penetration of confined ceramic targets has mainly been performed using phenomenological models such as the JH [10] model. The parameters of these models cannot be directly related to material properties such as yield strength and toughness. However, the micro-mechanical model used in this study does enable the effect of ceramic yield strength and toughness on the interface defeat velocity v_c to be explored. All calculations are presented for the reference target size with $L/a = 10$ and material parameters also held fixed at their reference values listed in Section 2.1.2 except for the yield strength σ_Y and toughness K_{IC} . These two parameters are varied and their effect on v_c is quantified. In order to make more direct contact with engineering values of these material properties we present the results directly in terms of σ_Y and K_{IC} rather than the corresponding non-dimensional quantities. Varying σ_Y of course implies that the material viscosity η and consequently ℓ_p is also varied and thus in these simulations ℓ_p/a is not held fixed while ℓ_D/a is fixed at its reference value.

Predictions of v_c as function of the yield strength σ_Y are included in Fig. 12a for three choices of the fracture toughness K_{IC} . The asymptotes for $\sigma_Y \rightarrow \infty$ are included in Fig. 12a for each of the three values of K_{IC} . There is a clear trend of increasing v_c with yield strength until the curves plateau at large σ_Y . Similarly, v_c increases with increasing K_{IC} for a given σ_Y though the effect of K_{IC} on the interface defeat velocity is more evident at higher σ_Y . These results are rationalised as follows. Penetration of the target occurs by the expansion of a spherical cavity from zero radius to the radius a of the long-rod as discussed in Section 4.1. This expansion occurs by plastic deformation of the ceramic or cracking of the ceramic (or a combination of both) and thus there is a general trend for an increase in v_c with increasing σ_Y and K_{IC} . At low σ_Y , the deformation is dominated by plasticity with nearly no cracking and hence v_c is insensitive to K_{IC} . Similarly, at high σ_Y the expansion of the cavity occurs primarily by cracking of the ceramic with no plasticity and hence v_c increases with increasing K_{IC} but is insensitive to σ_Y . Of course, the value of σ_Y above which there is

no further increase in v_c depends on K_{IC} with the asymptote in v_c being attained at $\sigma_Y \approx 20 \text{ GPa}$ for $K_{IC} = 1 \text{ MPa}\sqrt{\text{m}}$ but v_c is still increasing at this value of σ_Y in the $K_{IC} = 30 \text{ MPa}\sqrt{\text{m}}$ case.

These results are summarised in Fig. 12b where contours of v_c are included in a map with axes of yield strength σ_Y and toughness K_{IC} . Two key regimes are seen to emerge from the map: (i) *plasticity dominated* penetration where the contours of v_c are nearly vertical indicating little dependence on K_{IC} and (ii) *cracking dominated* penetration where the contours of v_c are nearly horizontal indicating little dependence on σ_Y . These two regimes are marked in Fig. 12b. The location of the Corbit-98 Alumina (properties listed in Section 2.1.2) is included in Fig. 12b: this “standard” Alumina lies at approximately the boundary of the two regimes. Increasing K_{IC} for this Alumina will have a relatively minor benefit in increasing the interface defeat velocity while an enhancement in the yield strength is predicted to have a greater benefit. We emphasise that this conclusion of increasing the yield strength to enhance penetration performance while true for the relatively low yield strength Alumina, is not expected to hold for high yield strength ceramics such as SiC where most likely the opposite will be true. Moreover, it remains unclear whether maximising performance in a Lundberg test will translate to performance enhancements in an armour system – such an investigation while critical is beyond the scope of this study.

5. Concluding remarks

The dynamic penetration of confined ceramic targets by Tungsten long-rod penetrators has been investigated via finite element (FE) calculations. The ceramic is modelled using a mechanism-based constitutive model that directly relates the ceramic behaviour to fundamental material properties such as strength and toughness. The computational model has been kept necessarily simple in so much as that the penetrator and the penetration through the outer casing is not explicitly modelled. Rather, loading due to the long-rod is approximated to be hydrodynamic and a pressure directly applied on the ceramic surface. This is done so as to focus on the penetration mechanisms into the ceramic and keep the general conclusions applicable to the wide variety of experiments reported in the literature rather than a specific situation. Nevertheless, three penetration regimes, viz. interface defeat, dwell followed by penetration and penetration with no or short dwell emerge from the calculations both when ceramic microcracking is included and excluded. In fact, the calculations demonstrate that penetration occurs by a spherical cavity expansion mode and thus continued penetration occurs when the

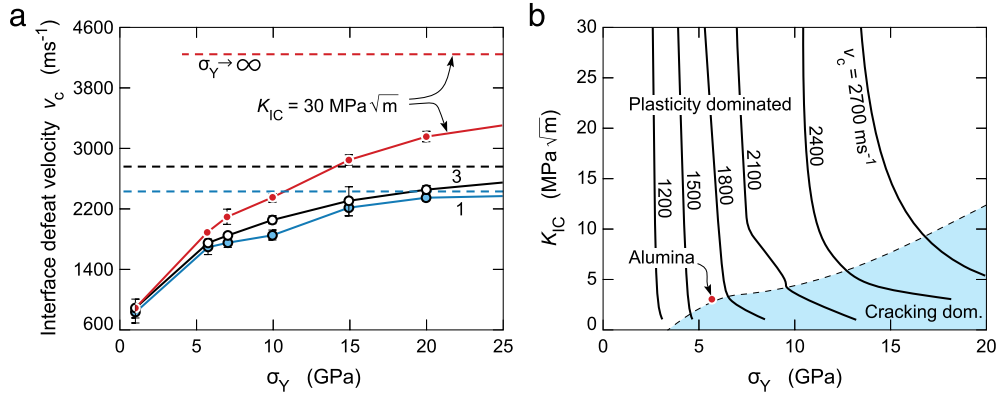


Fig. 12. (a) Predictions of the dependence of the interface defeat velocity v_c on the toughness K_{IC} and yield strength σ_Y for the $L/a = 10$ target. Results are shown for three values of K_{IC} with the asymptotic values of v_c in the limit $\sigma_Y \rightarrow \infty$ included for each K_{IC} . All other material properties are those for Alumina. (b) A map with axes of toughness K_{IC} and yield strength σ_Y to illustrate the plasticity and cracking dominated regimes of penetration. The map includes contours of v_c . The location of the Corbit-98 Alumina is marked on the map.

loading is sufficient to grow the inelastic zone (which could be either a plastic or a damage/comminuted zone) to a critical size. The dwell time is set by the time required to establish this critical size of the inelastic zone. The key role of comminution/damage is to reduce the pressure required for penetration. Moreover, the calculations show that the so-called fluid–structure interaction (FSI) effect resulting from the backflow of the deforming projectile is not essential for the existence of the three regimes of penetration.

The mechanism-based model includes three material length scales: (i) a lattice plasticity length scale related to material rate dependence; (ii) a damage length scale associated with the size of the comminuted zone required for granular flow to occur and (iii) a length scale associated with the rate dependence of granular plasticity. We demonstrate that the lattice plasticity and damage length scales are typically comparable to the penetrator radius and are therefore the source of the strong penetration size effect observed in experiments. In particular, in line with observations, the calculations predict that the interface defeat velocity increases, as the setup is scaled-down in a geometrically self-similar manner. This is because the wavelengths associated with deformation become large compared to the material length scales and this effectively strengthens the ceramic.

The FE calculations are also used to probe the influence of material strength and toughness on the interface defeat velocity. Two regimes of behaviour emerge from the calculations. At low strength, material toughness has a negligible influence with the penetration being plasticity-dominated while at high strengths microcracking governs penetration with toughness having a major effect but strength playing only a minor role. The commonly used Corbit-98 Alumina is shown to lie at the boundary between these two regimes at a location where increasing the strength of this Alumina will have a greater influence on enhancing the penetration resistance rather than increasing its toughness.

Acknowledgements

The Cambridge University authors acknowledge support from DSTL, UK while HW is grateful to the Office of Naval Research for support under Grant Number N00014-16-1-2699 managed by David Shifler.

Appendix. Summary of coefficients for the microcracking model

The coefficients A , B , C and E required to calculate K_I for the microcracking model are derived in Deshpande and Evans [17].

Here we list these formulae for the sake of completeness. The coefficients A and B are given as

$$A \equiv c_1 (c_2 A_3 - c_2 A_1 + c_3), \quad (\text{A.1})$$

and

$$B \equiv \frac{c_1}{\sqrt{3}} (c_2 A_3 + c_2 A_1 + c_3), \quad (\text{A.2})$$

where

$$c_1 = \frac{1}{\frac{\pi^2}{2^{3/4}} \left[\left(\frac{D}{D_0} \right)^{1/3} - 1 + \beta \sqrt{2} \right]}, \quad (\text{A.3})$$

$$c_2 = 1 + 2 \left[\left(\frac{D}{D_0} \right)^{1/3} - 1 \right]^2 \left(\frac{D_0^{2/3}}{1 - D^{2/3}} \right), \quad (\text{A.4})$$

and

$$c_3 = \pi^2 \left[\left(\frac{D}{D_0} \right)^{1/3} - 1 \right]^2, \quad (\text{A.5})$$

while

$$A_1 = \pi \sqrt{\frac{\beta}{3}} \left[(1 + \mu^2)^{1/2} - \mu \right], \quad (\text{A.6})$$

and

$$A_3 = A_1 \left[\frac{(1 + \mu^2)^{1/2} + \mu}{(1 + \mu^2)^{1/2} - \mu} \right]. \quad (\text{A.7})$$

In the above expressions, $\beta = 0.45$ is a coefficient introduced by Ashby and Sammis [29] to convert the exact two-dimensional wing crack solutions to a three-dimensional state while $\mu = 0.75$ is the friction coefficient between the crack faces as calibrated for Alumina by Gamble et al. [19]. The coefficients C and E are defined as

$$C = A + \gamma \sqrt{\frac{1}{\sqrt{2}} \left(\frac{D}{D_0} \right)^{1/3}}, \quad (\text{A.8})$$

while

$$E^2 = \frac{B^2 C^2}{C^2 - A^2}, \quad (\text{A.9})$$

with the parameter γ calibrated to recover the correct tensile strength of Alumina. This calibration sets it to be $\gamma = 2$.

References

- [1] P. Lundberg, R. Renstrom, B. Lundberg, Impact of metallic projectiles on ceramic targets: transition between interface defeat and penetration, *Int. J. Impact Eng.* 24 (2000) 259–275.
- [2] R. Renström, P. Lundberg, B. Lundberg, Stationary contact between a cylindrical metallic projectile and a flat target surface under conditions of dwell, *Int. J. Impact Eng.* 30 (10) (2004) 1265–1282.
- [3] M. Wilkins, Second Progress Report of Light Armor Program, Report No. UCRL-50349, Lawrence Livermore Lab, Livermore (CA), USA, 1967.
- [4] G.E. Hauver, E.J. Rapacki, P.H. Netherwood, R.F. Benck, Interface Defeat of Long-Rod Projectiles By Ceramic Armor, US Army Research Laboratory Report ARL-TR-3590, Aberdeen Proving Ground, MD, USA, 2005.
- [5] P. Lundberg, B. Lundberg, Transition between interface defeat and penetration for tungsten projectiles and four silicon carbide materials, *Int. J. Impact Eng.* 31 (7) (2005) 781–792.
- [6] C.E. Anderson, T.J. Holmquist, D.L. Orphal, T. Behner, Dwell and interface defeat on borosilicate glass, *Int. J. Appl. Ceram. Technol.* 7 (6) (2010) 776–786.
- [7] J.C. LaSalvia, J. Campbell, J.J. Swab, J.W. McCauley, Beyond hardness: ceramics and ceramic-based composites for protection, *J. Mech.* 62 (1) (2010) 16–23.
- [8] D.A. Shockey, A.H. Marchand, S.R. Skaggs, G.E. Cort, M.W. Burkett, R. Parker, Failure phenomenology of confined ceramic targets and impacting rods, *Int. J. Impact Eng.* 9 (3) (1990) 263–275.
- [9] J.C. LaSalvia, J.W. McCauley, Inelastic deformation mechanisms and damage in structural ceramics subjected to high-velocity impact, *Int. J. Appl. Ceram. Technol.* 7 (5) (2010) 595–605.
- [10] T.J. Holmquist, G.R. Johnson, The failed strength of ceramics subjected to high-velocity impact, *J. Appl. Phys.* 104 (1) (2008) 013533.
- [11] T. Behner, C.E. Anderson Jr., T.J. Holmquist, D.L. Orphal, M. Wickert, D.W. Templeton, Penetration dynamics and interface defeat capability of silicon carbide against long rod impact, *Int. J. Impact Eng.* 38 (6) (2011) 419–425.
- [12] P. Lundberg, R. Renström, O. Andersson, Influence of length scale on the transition from interface defeat to penetration in unconfined ceramic targets, *J. Appl. Mech.* 80 (3) (2013) 031804.
- [13] T. Uth, V.S. Deshpande, Unsteady penetration of a target by a liquid jet, *Proc. Natl. Acad. Sci. USA* 110 (2013) 20028–20033.
- [14] D.C. Drucker, W. Prager, Soil mechanics and plastic analysis or limit design, *Quart. Appl. Math.* 10 (1952) 157–165.
- [15] G.R. Johnson, W.H. Cook, A constitutive model and data for metals subjected to large strains, high strain rates and high temperatures, in: 7th Int Symp on Ballistics, The Netherlands, 1983, pp. 541–547.
- [16] T.J. Holmquist, C.E. Anderson, T. Behner, D.L. Orphal, Mechanics of dwell and post-dwell penetration, *Adv. Appl. Ceram.* 109 (2010) 467–479.
- [17] V.S. Deshpande, A.G. Evans, Inelastic deformation and energy dissipation in ceramics: A mechanism-based constitutive model, *J. Mech. Phys. Solids* 56 (2008) 3077–3100.
- [18] V.S. Deshpande, E.A.N. Gamble, B.G. Compton, R.M. McMeeking, A.G. Evans, F.W. Zok, A constitutive description of the inelastic response of ceramics, *J. Am. Ceram. Soc.* 94 (2011) s204–214.
- [19] E.A.N. Gamble, B.G. Compton, V.S. Deshpande, A.G. Evans, F.W. Zok, Damage development in an armor ceramic under quasi-static indentation, *J. Am. Ceram. Soc.* 94 (2011) s215–225.
- [20] B.G. Compton, E.A. Gamble, V.S. Deshpande, F.W. Zok, Damage development in an armor alumina impacted with ductile metal spheres, *J. Mech. Mater. Struct.* 7 (2012) 575–591.
- [21] C.C. Holl, E.A. Gamble, F.W. Zok, et al., Effect of design on the performance of steel-alumina bilayers and trilayers subject to ballistic impact, *Mech. Mater.* 91 (2015) 241–251.
- [22] R.A. Bagnold, Experiments on a gravity-free dispersion of large solid particles in a newtonian fluid under shear, *Proc. R. Soc. Lond. Ser. A Math. Phys. Eng. Sci.* 225 (1954) 49–63.
- [23] Z.P. Bažant, M. Jirásek, Nonlocal integral formulations of plasticity and damage: survey of progress, *J. Eng. Mech.* 128 (2002) 1119–1149.
- [24] V. Tvergaard, A. Needleman, Effects of nonlocal damage in porous plastic solids, *Int. J. Solids Struct.* 32 (1995) 1063–1077.
- [25] R. Subramanian, S.J. Bless, Penetration of semi-infinite AD995 Alumina targets by Tungsten long rod penetrators from 1.5 to 3.5 km/s, *Int. J. Impact Eng.* 17 (1995) 807–816.
- [26] R. Bishop, R. Hill, N. Mott, The theory of indentation and hardness tests, *Proc. Phys. Soc.* 57 (1945) 147–159.
- [27] R. Hill, *The Mathematical Theory of Plasticity*, Oxford University Press, London, 1950.
- [28] J.W. Hutchinson, Plasticity at the micron scale, *Int. J. Solids Struct.* 37 (2000) 225–238.
- [29] M.F. Ashby, C.G. Sammis, The damage mechanics of brittle solids in compression, *Pure Appl. Geophys.* 133 (3) (1990) 489–521.